

Superhydrophobic Drag Reduction for Turbulent Flows in Open Water

Muchen Xu^{1,*}, Andrew Grabowski,¹ Ning Yu,¹ Gintare Kerezyte¹, Jeong-Won Lee,¹
Byron R. Pfeifer,² and Chang-Jin “CJ” Kim^{1,3,4,†}

¹Mechanical and Aerospace Engineering Department, University of California, Los Angeles (UCLA),
Los Angeles, California 90095, USA

²Marina Aquatic Center, University of California, Los Angeles (UCLA), Marina Del Rey, California 90292, USA

³Bioengineering Department, University of California, Los Angeles (UCLA), Los Angeles, California 90095, USA

⁴California NanoSystems Institute (CNSI), University of California, Los Angeles (UCLA), Los Angeles,
California 90095, USA

 (Received 26 June 2019; revised manuscript received 4 November 2019; accepted 31 January 2020; published 23 March 2020)

Despite two decades of research, drag reduction with superhydrophobic (SHPo) surfaces has never been experimentally confirmed under the most coveted condition, i.e., high Reynolds number flows in open water, thus casting doubt on its ultimate impact. Here, we present large drag reductions (approximately 30%) by SHPo surfaces tested on the sea at Re_x estimated to be as high as 6.5×10^6 . To achieve success, we prepare $4 \times 7 \text{ cm}^2$ silicon samples of re-entrant microtrenches for maximum plastron retention and test them as a portion of hull surface underneath a motorboat using a custom-developed comparative shear sensor. The state of plastron on the sample surfaces are observed throughout the tests via a custom-made miniature underwater camera. The successful results attest the importance of microscopic nuances of SHPo surfaces for plastron retention and drag reduction, guiding directions for future applications.

DOI: [10.1103/PhysRevApplied.13.034056](https://doi.org/10.1103/PhysRevApplied.13.034056)

I. INTRODUCTION AND BACKGROUND

Friction drag contributes to 60%–70% of the total drag on cargo ships and roughly 80% on tankers [1]. Since marine shipping alone accounts for about 12% of world-transportation energy consumption [2] and emits about 15% of total global toxic gases of NO_x and SO_x [3], even a mild drag reduction on marine vessels would yield a significant impact on energy saving and environment protection. Superhydrophobic [SHPo, abbreviated to differentiate it from superhydrophilic (SHPi), superoleophobic, and the likes] surfaces have shown great promise with their ability to trap air within the surface microstructures and create an effective slip in water without supplying the gas continuously [4,5]. If large enough, the slippage may entail a drag reduction appreciable for many flow systems. However, the fragility of the trapped air (i.e., plastron) has been the main challenge for the use of SHPo surface in the most practical conditions, i.e., turbulent flows in open water [6–8]. The plastron loss is accelerated by the high shear of turbulent flows and further exacerbated by the hydrostatic pressure as well as many environmental variables [7]

inevitable in open-water tests. For turbulent flows, while numerical studies have shown definite drag reduction and brought insights into the drag-reducing mechanism [9–12], experimental studies have reported mixed results, varying from substantial to negligible drag reduction, and even drag increase.

Figure 1 summarizes the recent experimental studies of SHPo drag reduction in turbulent flows [13–29]. Since many different flow facilities are used, we compare the results using the friction Reynolds number on smooth surface $Re_\tau = u_\tau \cdot \delta / \nu$ by estimating it from the flow data in each report, similarly to Gose *et al.* [17], where u_τ is the friction velocity, δ is boundary layer thickness, and ν is kinematic viscosity. As a relevant trend for drag ratio, the effect of Reynolds number unveiled by numerical studies [9,10] has been observed in some experiments [15,24,27] but contradicted in some others [13,17,21]. Most importantly, all but one [13] experimental study were performed in a confined flow, e.g., water tunnel, whether internal or external. The few experiments performed in open water were only with toy boats (centimeters in length) at low speed ($<0.5 \text{ m/s}$) [30–32] and did not reach turbulent flows. So far, the only high Reynolds number SHPo experiment performed in open water [13] found drag reduction at low Reynolds numbers but drag increase at high Reynolds numbers due to the diminishing plastron. These inconsistent and discouraging experimental results

*morleyxjtu@gmail.com

†cjkim@ucla.edu

‡Present address: 17075 Thornmint Ct, San Diego, California 92127, USA.

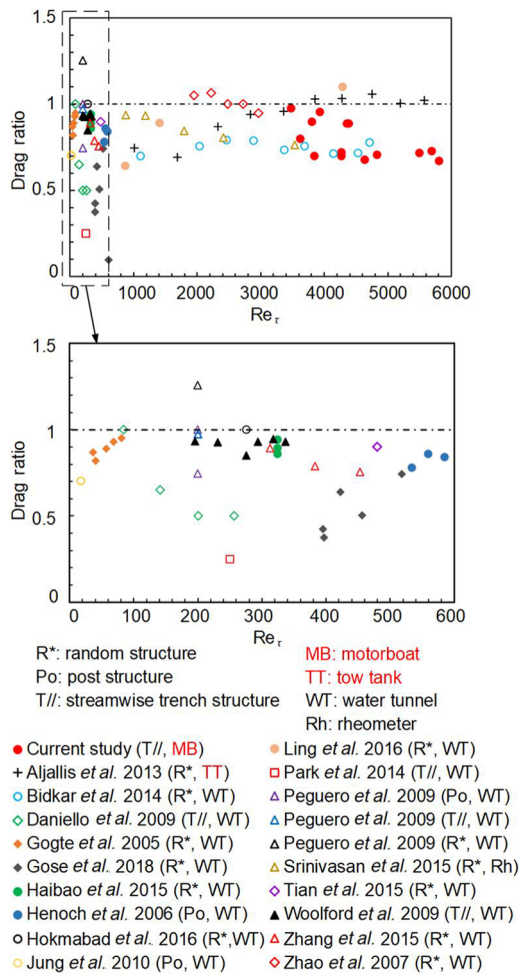


FIG. 1. Drag ratios (i.e., drag on target surface over drag on smooth surface) reported by the SHPo drag-reduction experiments in turbulent flows with the microstructure type and test condition indicated in parenthesis. Tow tank [13] and motorboat (this study) are the only tests performed in open water. For each study, the most representative results including the lowest drag ratio are converted to friction Reynolds number Re_τ for meaningful comparison, considering the widely different flow conditions. Most experiments are performed at $Re_\tau < 600$ and discernible in the magnified graph at the bottom.

after decades-long research have started to cast doubts on whether SHPo surfaces will ever bring the level of impact once anticipated [15,33].

Meanwhile, microcavities whose top edges are shaped to be “re-entrant” were shown to be more stable against wetting transition [34,35]. Because the loss of plastron has been the main culprit against a successful SHPo drag reduction for high Reynolds number flows in open water, in this paper we develop re-entrant microtrenches, which would provide a maximum plastron retention passively, i.e., without resorting to an active gas generation [36]. However, these well-defined sample surfaces, currently fabricated by MEMS technology for scientific studies,

are limited in size to fit within the 10-cm-diameter silicon wafer for us. To test a centimeter-size sample on an approximately 4-m-long boat, i.e., without having to cover the entire hull with the sample, a unique shear sensor developed for this purpose is utilized. After installing the shear sensor underneath a six-passenger motorboat, we succeed in performing desired flow experiments on open water, obtaining large drag reductions (around 30%, as high as 40%) in an actual marine environment at the high Reynolds numbers of practical interest (up to $Re_x \sim 6.5 \times 10^6$ or $Re_\tau \sim 6000$).

II. PREPARATION OF SHPo SURFACE SAMPLES

A. SHPo surface-sample design

Contrary to the commonly held impression, the large contact angles of highly SHPo surfaces are not strongly correlated to large slip, as explained in Ref. [8]. Rather, to obtain an appreciable drag reduction one needs a proper microstructure capable of both (i) producing a large-slip length and (ii) maintaining plastron persistently. First, for the large slip, following the SHPo studies in laminar flows for large-slip length [37], we choose to use SHPo surfaces with parallel microtrenches along the flow direction, as shown in Fig. 2(a). In addition, the experience with such surfaces in turbulent flows [22] suggested that a pitch (P) of $100 \mu\text{m}$ and a gas fraction (GF) around 90% are large enough for significant drag reduction. Since the $1 \times 2 \text{ cm}^2$ SHPo samples used in Ref. [22] were found to overestimate the drag reduction by 5–20% [38], in this study we

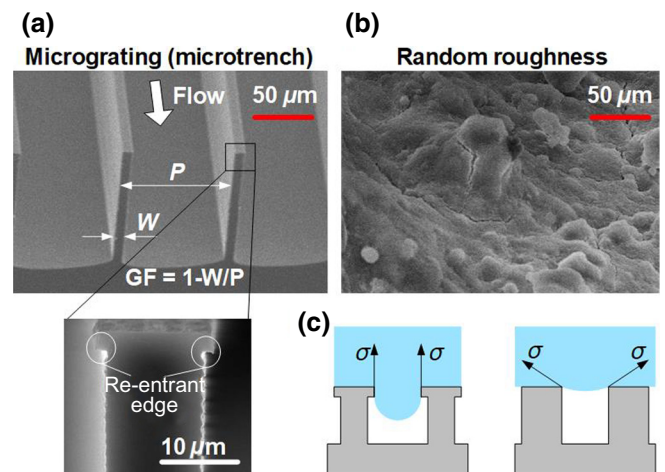


FIG. 2. Scanning electronic microscope (SEM) images of (a) a SHPo surface with re-entrant microtrenches (shown: $100\text{-}\mu\text{m}$ -pitch sample) tested for drag reduction and (b) a random roughness SHPo surface tested identically for comparison. (c) Schematic drawings to compare the wetting resistance between re-entrant (left) and regular (right) edges. For a hydrophobic material, the capillary force σ could point straight upward on re-entrant edges, maximizing the ability to resist depinning and maintain plastron.

use $4 \times 7 \text{ cm}^2$ SHPo samples, which are large enough to represent macro applications with negligible size effect. Because most of the experimental studies of SHPo drag reduction for turbulent flows, especially at high Reynolds numbers, used random roughness in the literature, we also prepare random structures similar to Ref. [13,19,27] for direct comparison [Fig. 2(b)]. Second, for the stable plastron, the microfabrication process is developed to obtain microtrenches whose top edges are re-entrant; see the inset picture of Fig. 2(a). The upward capillary force of the air-water interfaces, which helps retain the plastron, are larger on the re-entrant trenches than on the simple trenches (by approximately 2 times, assuming the intrinsic contact angle is 120°), as schematically explained in Fig. 2(c) [35]. As a result, the critical immersion depth, which is defined as the maximum depth where indefinite plastron is possible [7,39], would be increased similarly, helping the plastron persist better against all adversities. Because the drag-reducing ability is significantly compromised as soon as the meniscus is depinned from the top edge [8], the increased resistance to the meniscus depinning on the re-entrant trenches is considered more important for drag reduction than the commonly defined plastron lifetime [7,40].

B. SHPo surface-sample fabrication

The SHPo surface samples with parallel microtrenches are fabricated, starting with a 4-inch-diameter, $500\text{-}\mu\text{m}$ -thick, (100) silicon wafer covered with $1\text{-}\mu\text{m}$ -thick silicon dioxide, as summarized in Fig. 3. The silicon dioxide is patterned by photolithography and reactive-ion etching (RIE), and the resulting oxide patterns serves as a mask for the subsequent deep reactive-ion etching (DRIE), which digs microtrenches into the silicon substrate. The

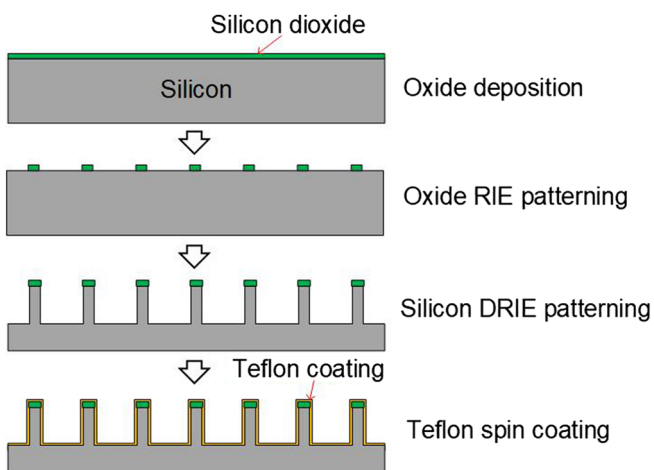


FIG. 3. Microfabrication process of trench SHPo surface. The processed wafer is diced to $4 \times 7 \text{ cm}^2$ rectangular sample before the Teflon-coating step.

thin oxide also renders the top edges of the trenches re-entrant by the slight undercut occurring during the DRIE, as shown in the inset of Fig. 2(a). After being cleaned by oxygen plasma to remove the polymer residues, the wafer is coated with an approximately $2\text{-}\mu\text{m}$ -thick photoresist (AZ 5214) and diced to a rectangular shape ($40 \times 70 \text{ mm}^2$) using high-speed dicing saw (Disco DAD321). The photoresist protects the wafer surface from getting dirty or damaged during the dicing. After dicing, the photoresist is dissolved and sample cleaned using oxygen plasma and Piranha solution (98 wt % sulfuric acid : 30 wt % hydrogen peroxide = 4:1). Finally, 2 wt % Teflon AF 1600 (DuPont) is spin coated on the sample and baked in two stages (165°C for 15 min and 330°C for 10 min, following the manufacturer's specifications) to a thickness around 200 nm [41]. Additional submicron details and fabrication techniques of microtrenches with re-entrant top corners [42,43] are beyond the current scope.

The SHPo surface samples with random structures are prepared using a two-step coating process with commercial SHPo spraying product (NeverWet®, Rust-Oleum, LLC) following product manual [44]. The product is a sprayable blend of hydrophobic silica nanoparticles embedded within a silicone matrix [45] forming SHPo surfaces. This type of random-roughness SHPo surface is used in most of the drag-reduction studies summarized in Fig. 1.

III. INSTRUMENTATION AND EXPERIMENTS

A. Low-profile comparative shear-stress sensor

To make sure the test samples are subjected to the flow conditions of an actual boat, our approach is to replace a portion of the immersed hull surface of the boat with the test sample developed above. Since the main challenge for drag reduction is with high Reynolds number flows according to the only open-water turbulent-flow tests so far [13], we take the challenge by placing the sample near the stern where the Reynolds number would be the largest. If a SHPo surface could maintain the plastron and produce a considerable drag reduction on the aft region of the boat, the same surface would likely maintain the plastron and produce drag reduction on most other regions as well. Since no existing shear sensor works under our desired condition, we develop a shear-sensing system, which is detailed in Ref. [42,46] but described briefly here for basic information.

The sensor includes two floating elements each suspended from the main plate by highly flexible but robust beams, all monolithically manufactured from one metal plate, as shown in Fig. 4(a). One floating element mounts a SHPo sample (target surface), and the other mounts a smooth sample (reference surface). When flow exerts shear stress on the sample surfaces, the floating elements shift, and their shifting distances are measured by two high-resolution optical encoders held in the encoder plate, as

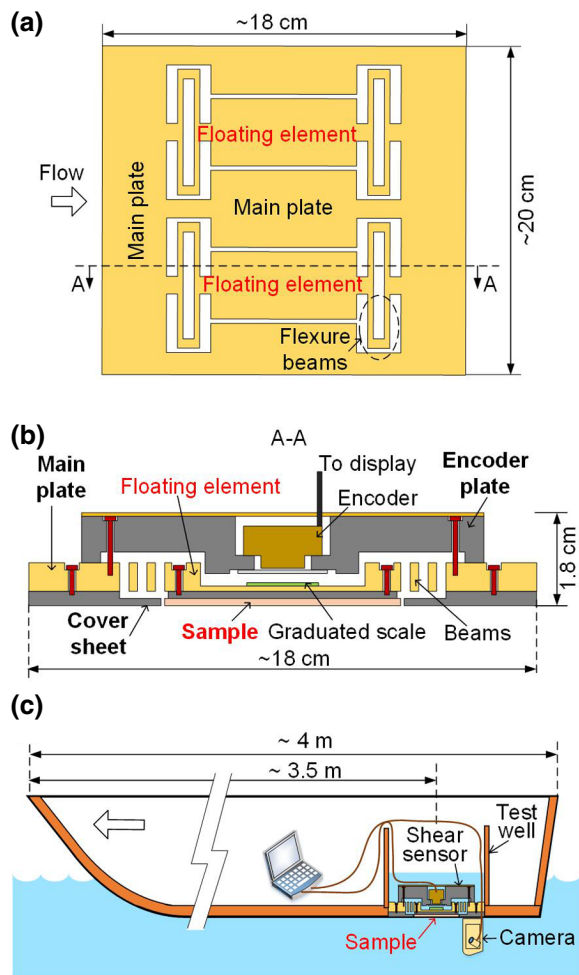


FIG. 4. Low-profile comparative shear sensor and testing setups (drawn not to scale). (a) Schematic top view of the sensor shows two identical floating elements defined within the main plate. (b) Schematic cross-section view of the sensor shows the low-profile design by two plates (main and encoder plate). (c) Schematic cross-section view of the boat shows a test well installed near the stern. Note the underwater camera to observe the sample surface during flow tests.

shown in Fig. 4(b). By comparing the two displacements, one can accurately obtain the relative shear force, i.e., drag ratio of the target surface to the reference. The flexure beams are machined to form a high thickness-to-width aspect ratio against out-of-plane deformation (e.g., 10 mm thick to 0.5 mm wide) and a very low width-to-length ratio against in-plane deformation in one direction (e.g., 0.5 mm wide to 25 mm long), ensuring the floating elements are compliant in the flow direction but safely rigid in all other directions. As a result, the sensor is only sensitive to shear force in the streamwise (parallel to flow) direction and insensitive to forces in both the spanwise (traverse to flow) and out-of-plane (vertical from the wall) directions. Because the structures of the plate needed for this study are too large or fragile for MEMS fabrication

while too flexible or costly for existing machining techniques including wire electro-discharge machining (EDM) even with high-end equipment and professional services, a machining process has to be newly developed, as explained in Ref. [42,46]. The size of the floating element and the dimensions of the flexure beams are determined by the available sample sizes and desired shear range.

The two sample surfaces are fixed onto—or underneath, if the upside-down orientation of Figs. 4(b) and 4(c) is followed blindly—the two floating elements, and a cover plate is fixed onto (or underneath) the main plate, as shown in Fig. 4(b). Intricate provisions are developed to ensure the top surfaces (i.e., the surfaces in contact with water) of the samples are flush (within $5\ \mu\text{m}$) with the top surface (in contact with water) of the surrounding cover plate in order to prevent the measurement error that may be caused by small steps [14,47]. Also, the gap between the sample surfaces and the surrounding cover plate are minimized using a feeler gauge to further prevent measurement error.

Once the spring constants of the beams are measured for calibration after machining, the shear stress on each floating element can be calculated by reading its displacement in flows. As shown in Fig. 4(b), an optical encoder (M2000 linear encoder, Celera Motion, Inc.) is used to measure the displacement, using a graduated scale attached on the back of the floating element. Based on Talbot effect, the optical encoder employed measures the displacement with resolution as high as 78 nm. More details of the shear-sensor development and characterization can be found in Ref. [42,46]. As shown in Fig. 4(c), the shear sensor is installed underneath a six-passenger motorboat to measure the drag ratio between the two samples attached on two floating elements. Although the current shear sensor is developed mostly to measure drag ratios in the current study, it can also measure the shear-force value on each of the floating elements by calibrating them under known flows.

B. Boat retrofitting

All boat tests have been conducted in Marina Del Rey, California, USA on relatively calm water. The boat used for this study is a 13' (13'4" or 4.06 m long to be accurate) 1979 Boston Whaler propelled by a 20-horsepower outboard engine (Honda), as pictured in Fig. 5(a). The hull is made of a 2–3-cm-thick outer layer of fiberglass, a 7–8-cm-thick middle layer of closed-cell foam that provides buoyancy, and another layer of fiberglass on the inside of the boat. As shown in Fig. 5(a) and drawn in Figs. 4(c) (not to scale) and 5(b) (to scale), a “test well” is developed and located near the stern on the portside of the keel axis. To make the test well, firstly, the hull of the boat is machined to open a rectangular hole ($24 \times 22\ \text{cm}^2$). The four sidewalls of the test well are made with reinforced wood board, and a holder plate for the shear sensor is CNC

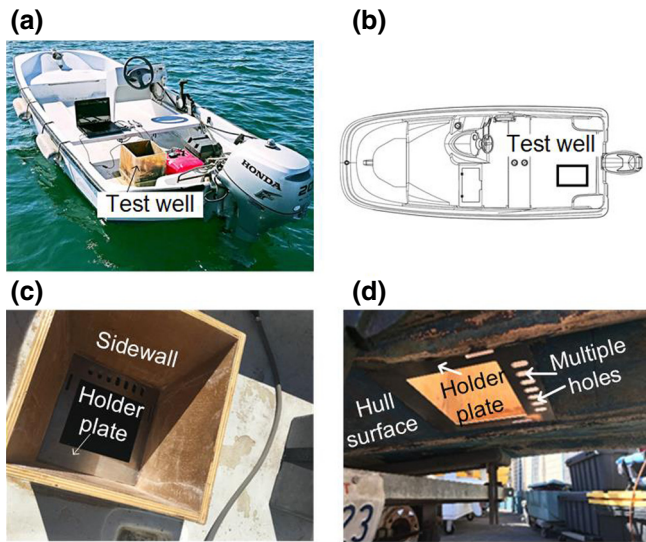


FIG. 5. Modification of the boat to install a test well, in which the shear sensor is placed at the bottom. (a) Picture of the boat. (b) Schematic of the boat indicating the location of the test well. (c) Test well placed on the hole, viewed from above the boat. The holder plate for the shear sensor is seen at the bottom of the test well. (d) The holder plate at the bottom of test well, viewed from under the boat. The shear sensor is placed at the opening and attached to the holder plate.

machined from an anticorrosion aluminum plate. After attaching the holder plate to the bottom end of the side-walls, as shown in Fig. 5(c) (pictured from above), the completed test well is placed into the rectangular hole to make the holder plate level with the hull surface in water, as shown in Fig. 5(d) (pictured from under the boat while outside the water). The holder plate has multiple holes to let the water pass into and out of the test well freely so that hydrostatic pressure does not build on the shear sensor. The multiple holes are placed downstream of the shear sensor so that the water through them does not affect the main water flow over the sample surfaces. The gap between the holder plate and the fiberglass hull bottom is filled with marine adhesive, and the bottom surfaces are then polished to make them flush and smooth. In addition, the underwater camera is attached to the bottom of the test well immediately downstream of the target surface to continually monitor its plastron state, as indicated in Fig. 4(c).

C. Flow tests with the shear sensor under the boat

The shear-stress sensor developed above records the shear force exerted on each floating element with sampling frequency of 512 Hz. During each run in the boat test, the shear-force data are streamed during the entire run, i.e., from before accelerating the boat to after stopping the boat. One exemplary dataset is presented in Fig. 6(a) for a SHPo surface with 100- μm pitch and 90% gas fraction. Figure 6(a) shows the original 512-Hz data for both

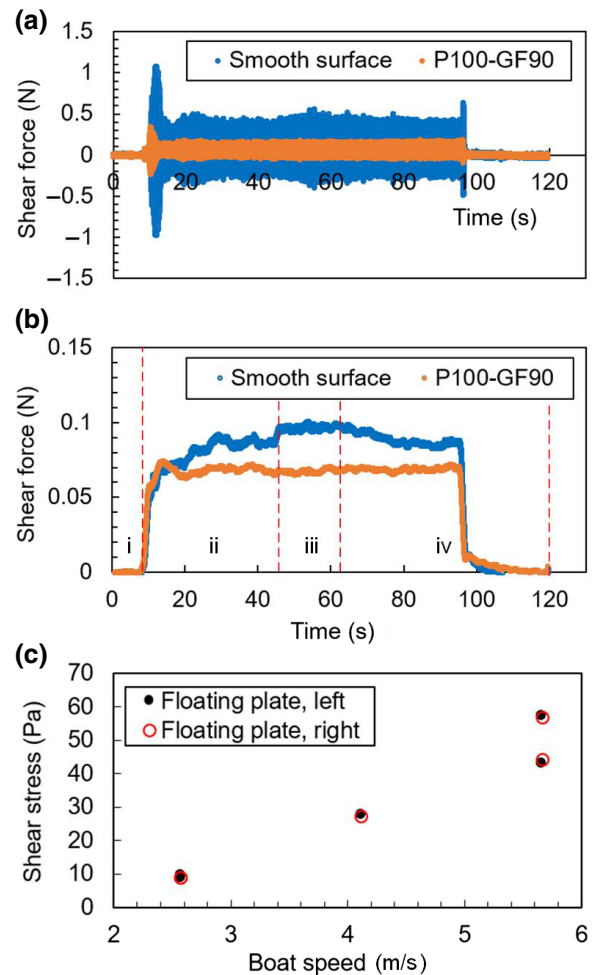


FIG. 6. Temporal shear-force data (a),(b) and confirmation of comparative measurement (c). (a) Raw shear-force data from the shear-stress sensor. (b) Filtered shear-force data reveals (i) stationary, (ii) acceleration, (iii) steady, and (iv) deceleration stage. The drag ratio is obtained by comparing the two values averaged during the steady stage. (c) Shear stresses on the two floating elements covered with two of the same smooth surfaces confirms they are identical.

the reference (smooth) surface and the target (SHPo) surface, which are placed side by side with their shear forces measured simultaneously. In addition to the smaller drag, the SHPo surface showed smaller fluctuation compared with the smooth surface, corroborating a previous study [22]. Figure 6(b) shows the filtered data by applying moving averages of a 1-s window. From Fig. 6(b), different stages of a boat-test run can be clearly seen: (i) stationary, (ii) acceleration, (iii) steady, i.e., constant speed, and (iv) deceleration. The drag ratios are obtained by comparing the shear forces of SHPo and smooth surface in stage (iii), where the boat maintained a constant speed. To complete each test run with a straight travel path (i.e., no turns in order to minimize flow variations) on a relatively calm water under the circumstance (e.g., traffic of other boats),

we let a steady stage last about 15–20 s, which turned out sufficiently long for our purpose. From the dataset exemplified in Fig. 6(b), the error range of each data point was found to be $\pm 5\%$.

To verify that the two floating elements on the comparative shear sensor experience the same flow condition during boat test, we have conducted an experiment using two of the same smooth samples mounted on the two floating elements. Figure 6(c) presents the shear stresses measured at three different boat speeds, showing the difference between the two floating elements are very small. Considering the random and uncontrolled nature of the external flows under the boat operated in marine environment with wind and other boats, the close data between the two different boat tests indicate the two floating elements placed next to each other, when tested together, experience practically the same flow condition, confirming the utility of the comparative shear sensor.

D. Estimation of Reynolds number of boat testing

To calculate the Reynolds number $Re_x = UL/\nu$ on the sample surfaces during the boat tests, the wetting length of the boat L needs to be known as well as the boat speed U . The boat speed U is measured using a boat speedometer (Raymarine i40). However, the wetting length L cannot be measured easily because it changes with the boat speed, as shown in Fig. 7, as well as other factors, such as the weight and distribution of the passengers. Accordingly, we obtain the wetting length L for every data point, as explained in Fig. 7. The friction Reynolds number Re_τ is then calculated from Re_x using the following boundary layer theory [48]:

$$Re_\tau = \frac{\delta u_\tau}{\nu} = 0.37 Re_x^{0.8} \sqrt{\frac{C_f}{2}},$$

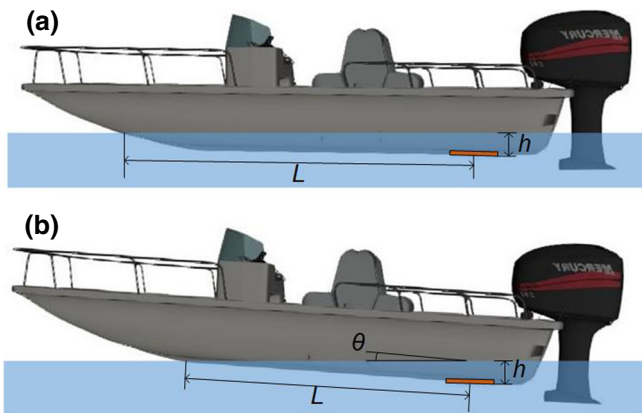


FIG. 7. Geometric estimation of the wetting length L by measuring the immersion depth h and bow-up angle θ for every run during the boat tests. (a) Boat at rest. (b) Boat at high speed.

where C_f is the skin friction coefficient calculated from the shear stress measured directly on the smooth sample.

E. Miniature underwater camera system

To interpret the drag data on a SHPo surface properly, it is crucial to monitor the plastron on it during the flow experiments. It is relatively easy to monitor the sample surface during lab experiments, where the sample is stationary in an experimental setup designed to allow viewing. However, for open-water tests, where samples move at a high speed, one would need a video camera installed near the surface of interest and traveling with the surface underwater. The camera developed for the high-speed flow tests in this paper is: (1) of a small size to minimize the form drag when traveling with the sample surface through water, (2) adjustable for its focal length to accommodate varying setup dimensions, (3) capable of real-time imaging to spot potential problems immediately during the test, and of course (4) waterproof for the depth and speed of the flow tests. Since no such underwater camera system is found available commercially, we develop our own system shown in Fig. 8, consisting of a miniature camera sealed in a waterproof camera case, which is, in turn, placed in a streamlined camera housing.

Since no commercial waterproof camera is small enough for our needs, we chose a regular (i.e., not waterproof) spy camera (Adafruit) designed for Raspberry Pi computer just for its small size (8.5 mm long, 7.4 mm in diameter). The waterproofness and focal-length adjustment are achieved by developing a camera case based on the popular Geocache Container (Geocache Nation). An aluminum “nano” Geocache container (14 mm tall and 11 mm in diameter) is chosen for its small size and screw-top design, where an O-ring can be inserted. The focal length of the miniature camera can be adjusted inside the camera case, when

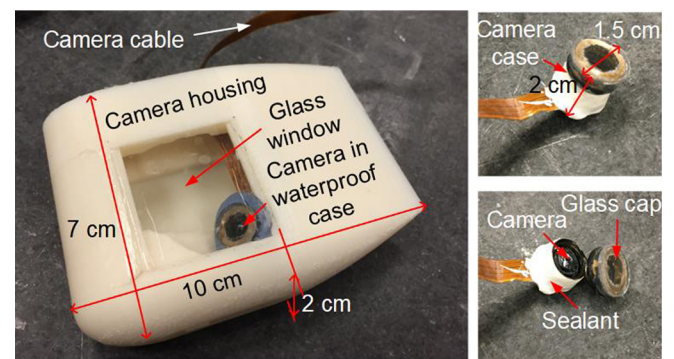


FIG. 8. Underwater camera system developed for real-time SHPo surface monitoring. The camera case is developed to meet the IP28 specification, and the camera housing is streamlined to minimize the drag.

necessary, by opening the screw top of the case, twisting the camera lens, and closing the screw top of the case to reseal. The waterproof camera case with the camera inside is, then, placed inside the camera housing, whose cross section is streamlined (i.e., symmetrical four-digit NACA airfoil) to minimize the form drag. The approximately 2-cm-wide, 7-cm-high, and 10-cm-long camera housing is 3D printed (Stratasys Dimension Elite) using a thermoplastic (acrylonitrile butadiene styrene or ABS) with enough inner space to adjust the camera case to desired viewing angles. The camera is connected via a 2-m-long ribbon cable to the main Raspberry Pi computer, which is controlled remotely from a laptop computer via Ethernet cables and a router. Once the camera system is immersed in water, the glass window on the camera housing is opened to fill its inner space with water to avoid any image distortion and closed using a thin rubber band.

A key to the waterproof system is the engineering of the camera case, starting with the nano Geocache container. First, in order to insert the camera into the container and make its top transparent, the two ends of the Geocache container are machined off on a lathe. A 7/16" collet is used to hold the empty container while a 19/32" drill bit made a through-hole. Then, a straight-edge knife tool cuts the remaining top surfaces until the surface is smooth. The bottom end of the Geocache container is attached onto the camera board with super glue and sealed with 3M Marine Adhesive Sealant 5200 Fast Cure, which is a polyurethane adhesive suitable for metal-plastic sealing. The top end of the container is covered by a piece of ultra-high temperature quartz glass (1/2" diameter, 1/16" thickness) purchased from McMaster-Carr. The glass-metal contact is sealed with West Marine polyether multicaulk sealant. The assembly is left in room temperature for five days before it can be used for underwater flow tests. This camera case is developed to be IP28 (based on the International Protection Marking or Ingress Protection Marking chart), which means protecting a large surface of body in water deeper than 1 m for more than 30 min. To counter for the low manufacturing yield and poor usage durability by the manual fabrication in our research lab, we produce enough camera cases (over 10 units) that are confirmed durable at 2 bars (i.e., approximately 20 m deep) of hydrostatic pressure for over 2 h, exceeding IP28, to complete the experiments for this study. Since the water sealing deteriorated after an extended underwater usage due to the poor quality control of the manual manufacturing in the lab, we end up expending multiple camera systems to complete the current study.

Movie S1 within the Supplemental Material [49] is an example of what an operator would observe live while testing a trench SHPo sample. The optical images (i.e., silvery or dark) from the custom-developed underwater camera provide the first-order information whether the plastron is intact or lost although they do not reveal further details,

such as whether the liquid-air-solid line has slid into the trench and compromised the drag reduction [6–8].

IV. RESULTS AND DISCUSSION

With the boat and shear sensor described above, SHPo drag-reduction experiments have been performed for turbulent flows on the sea. Figure 9(a) summarizes the results of all drag-reduction experiments. In the figure, each data point represents the average value (with the $\pm 5\%$ error bars not included for visual clarity) over 15–20 s of steady speed maintained for each test run as explained in Sec. III C and Fig. 6. The friction Reynolds number Re_τ shown in the graph is estimated from the boat speed, boat wetting area, and shear stress on the smooth surface measured with the shear sensor, as explained in Sec. III D. Due to the bow up of the boat at high speeds leading to a smaller wetted area and length, as illustrated in Fig. 7, Re_τ does not necessarily increase with boat speed but often rather decreases with speed. Accordingly, the regular Reynolds number Re_x added on the graph top should be used only as a rough guideline in relation to the friction Reynolds number Re_τ .

Three trench SHPo surfaces [Fig. 2(a)] with three different pitches ($P = 50, 100, 200 \mu\text{m}$) and one gas fraction (GF = 90%) have been tested, as well as one random roughness SHPo surface for comparison in Fig. 9(a). The surface with $P = 100 \mu\text{m}$ provided the best overall performance with the drag ratio dropping to around 0.7 (i.e., 30% drag reduction) consistently for Re_τ between 4300 and 5800. Meanwhile, a substantially uniform plastron was observed on its surface for Re_τ between 3600 and 5800 (Re_x roughly estimated to be between 4.5×10^6 and 6.5×10^6) or speed between 5 and 10 knots (2.57 and 5.14 m/s). The surface with $P = 200 \mu\text{m}$, which is capable of a larger slip length [37], dropped the drag ratio to as low as 0.6 (i.e., 40% drag reduction) at $Re_\tau \sim 4400$ with a healthy plastron but lost the advantage at lower Re_τ as small bubbles attached on the plastron added a form drag. The surface with $P = 50 \mu\text{m}$ maintained a stable plastron throughout the tests but dropped the drag ratio to only as low as 0.8 (i.e., 20% drag reduction) because its slip length is inherently smaller [37]. Figure 9(a) suggests a trend of the slip length or drag reduction increasing with Re_τ or GF. Previous numerical studies [38,50] showed the slip length in viscous unit b^+ or drag ratio would depend on the shear-free interface d in viscous unit $d^+ = d/\delta_v = (P \times \text{GF})/(v/u_\tau)$, where δ_v is the viscous length (wall unit). Note u_τ can be calculated from the wall shear stress on SHPo surfaces measured by the shear sensor. Since d^+ increases with Re_τ or GF based on its definition, Fig. 9(a) essentially verifies that b^+ increases with d^+ .

Unlike the SHPo surfaces with trenches above [Fig. 2(a)], those with random structures [Fig. 2(b)] led to a drag increase, confirming the previous study by Aljallis

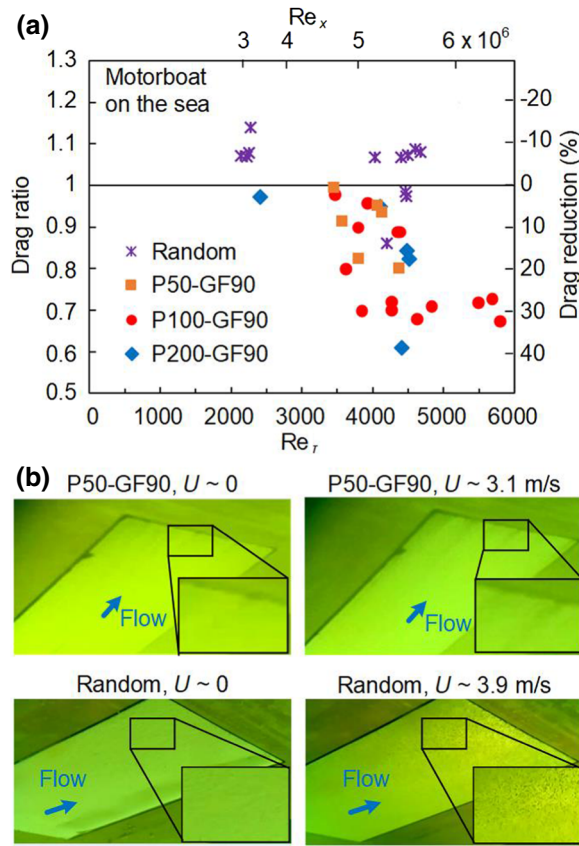


FIG. 9. Results (a) Drag ratio of SHPo surfaces (with respect to smooth surface) obtained from boat tests in open water. P and GF indicate the pitch (μm) and gas fraction (%) of the trench structures, respectively, and ‘Random’ represents the random roughness structure. The x -axis is scaled for the friction Reynolds number Re_τ , and the corresponding regular Reynolds number Re_x is marked on top of the graph. Despite the uncontrollable field conditions, trench surface with 100 μm pitch and 90% gas fraction (shown in red) provided a stable drag reduction of approximately 30% between a boat speed of 3–4 m/s. (b) Snapshots of SHPo surfaces during boat tests. The trench SHPo surface with $P = 50$ μm and $GF = 90\%$ maintained a plastron both when stationary and at high speed in the current test (also watch Movie S1 within the Supplemental Material [49]). In contrast, the SHPo surface with random structures maintained a thick plastron when stationary but showed numerous black dots at high speed (also watch Movie S2 within the Supplemental Material [49]), indicating their tall asperities penetrated into the water. The form drag by the penetration overshadowed the drag reduction by the remaining plastron, resulting in the overall drag increase.

et al. [13]. This drag increase could be explained from the gas depletion at high speed, as observed in the bottom two pictures of Fig. 9(b) and Movie S2 within the Supplemental Material [49]. While the SHPo surface with random roughness was covered with a thick plastron at rest ($U \sim 0$ m/sec), at $U \sim 3.9$ m/sec the plastron was thinned and numerous roughness peaks impaled into the water, creating numerous black dots. This penetration introduces

a form drag [8,14,17,51], and leads to an overall drag increase. Even the many air bubbles found passing by the SHPo surface could not prevent the loss of plastron. In stark contrast, the plastron persisted dramatically better on the trench SHPo surface developed for this study [Fig. 2(a)], i.e., made of re-entrant trenches aligned parallel to the streamline direction, as observed in the top two pictures of Fig. 9(b) as well as Movie S1 within the Supplemental Material [49], most likely because the trench tops are flat (i.e., of uniform height) with no asperities. The direct relationship between the state of the observed plastron and the amount of measured drag reduction confirms that plastron plays the key role in SHPo drag reduction, as reviewed in Ref. [8]. Because the boat bottom is in shallow water, which is saturated with air [7], and frequently bumped with the entrained bubbles, and the gas stability is maximized in the re-entrant microtrenches, the plastron was mostly retained on the trench SHPo samples during the tests and provided successful drag reduction. In comparison, the same surfaces with regular (i.e., no re-entrance) microtrenches showed widely unpredictable plastron retainment and did not lead to any repeatable drag reduction in the current boat experiments. Since the shallow immersion in bubble-containing water is quite common for many small watercrafts, the passive SHPo surfaces are expected to enjoy ample utilities before the semiactive SHPo surfaces [36] become available for field studies.

V. SUMMARY

We have obtained significant (typically around 30%, up to 40%) drag reductions on a macroscale (>1 m) object traveling at high speeds (5–10 knots) on open water, confirming the drag-reducing capabilities of SHPo surfaces in flows of practical interest. The results showed such a goal can be achieved only with properly designed SHPo surfaces, explaining why SHPo drag reduction in open water has been so elusive with random roughness SHPo surfaces. Although the current study was performed with a 4×7 cm^2 SHPo sample on a 13 foot boat for practical reasons, similar SHPo surfaces in a large area would benefit a wide range of watercrafts, from surfboards to vessels, by increasing the top speed or saving propulsion energy. Mass manufacturing of the SHPo surfaces in this study is feasible and under development [42,43], although technological and economical challenges are abundant. Finally, it is important to note that SHPo drag reduction can be considered for a wide range of applications, whenever there is a need to apply the technology for friction reduction of liquid flows, including pipe flows.

ACKNOWLEDGMENTS

The authors appreciate the discussions with John Kim and assistance from Hao Tong and UCLA Marine Aquatic Center, as well as the review of the manuscript by

John Kim and Bruce Dunn. This work is supported by DARPA HR0011-15-2-0021, NSF CBET 1336966, ONR N000141110503, and NSF CMMI 1720499, as well as UCLA Graduate Fellowship (N.Y.), Volgenau Chair (C.-J.K.) and Faculty Research Grant (J.-W.L.).

-
- [1] K. Fukuda, J. Tokunaga, T. Nobunaga, T. Nakatani, T. Iwasaki, and Y. Kunitake, Frictional drag reduction with air lubricant over a super-water-repellent surface, *J. Mar. Sci. Technol.* **5**, 123 (2000).
- [2] M. Lynes, International energy outlook 2016: transportation sector, Report No. DOE/EIA-0484, 2016.
- [3] T. W. P. Smith, *et al.*, *Third IMO Greenhouse gas Study 2014* (International Maritime Organization, London, UK, 2015), p. 2.
- [4] J. P. Rothstein, Slip on superhydrophobic surfaces, *Annu. Rev. Fluid Mech.* **42**, 89 (2010).
- [5] C.-H. Choi and C.-J. Kim, Large Slip of Aqueous Liquid Flow Over a Nanoengineered Superhydrophobic Surface, *Phys. Rev. Lett.* **96**, 066001 (2006).
- [6] L. Bocquet and E. Lauga, A smooth future?, *Nat. Mater.* **10**, 334 (2011).
- [7] M. Xu, G. Sun, and C.-J. Kim, Infinite Lifetime of Underwater Superhydrophobic States, *Phys. Rev. Lett.* **113**, 136103 (2014).
- [8] C. Lee, C.-H. Choi, and C.-J. Kim, Superhydrophobic drag reduction in laminar flows: A critical review, *Exp. Fluids* **57**, 176 (2016).
- [9] T. G. Min and J. Kim, Effects of hydrophobic surface on skin-friction drag, *Phys. Fluids* **16**, L55 (2004).
- [10] J. Lee, T. O. Jelly, and T. A. Zaki, Effect of Reynolds number on turbulent drag reduction by superhydrophobic surface textures, *Flow Turbul. Combust.* **95**, 277 (2015).
- [11] A. Rastegari and R. Akhavan, The common mechanism of turbulent skin-friction drag reduction with superhydrophobic longitudinal microgrooves and riblets, *J. Fluid Mech.* **838**, 68 (2018).
- [12] I. Arenas, E. García, M. K. Fu, P. Orlandi, M. Hultmark, and S. Leonardi, Comparison between super-hydrophobic, liquid infused and rough surfaces: A direct numerical simulation study, *J. Fluid Mech.* **869**, 500 (2019).
- [13] E. Aljallis, M. A. Sarshar, R. Datla, V. Sikka, A. Jones, and C. H. Choi, Experimental study of skin friction drag reduction on superhydrophobic flat plates in high Reynolds number boundary layer flow, *Phys. Fluids* **25**, 025103 (2013).
- [14] R. A. Bidkar, L. Leblanc, A. J. Kulkarni, V. Bahadur, S. L. Ceccio, and M. Perlin, Skin-friction drag reduction in the turbulent regime using random-textured hydrophobic surfaces, *Phys. Fluids* **26**, 085108 (2014).
- [15] R. J. Daniello, N. E. Waterhouse, and J. P. Rothstein, Drag reduction in turbulent flows over superhydrophobic surfaces, *Phys. Fluids* **21**, 085103 (2009).
- [16] S. Gogte, P. Vorobieff, R. Truesdell, A. Mammoli, F. van Swol, P. Shah, and C. J. Brinker, Effective slip on textured superhydrophobic surfaces, *Phys. Fluids* **17**, 051701 (2005).
- [17] J. W. Gose, K. Golovin, M. Boban, J. M. Mabry, A. Tuteja, M. Perlin, and S. L. Ceccio, Characterization of superhydrophobic surfaces for drag reduction in turbulent flow, *J. Fluid Mech.* **845**, 560 (2018).
- [18] C. Henoeh, T. Krupenkin, P. Kolodner, J. Taylor, M. Hodes, A. Lyons, C. Peguero, and K. Breuer, in *3rd AIAA Flow Control Conference* (AIAA, San Francisco, 2006), p. 3192.
- [19] B. V. Hokmabad and S. Ghaemi, Turbulent flow over wetted and non-wetted superhydrophobic counterparts with random structure, *Phys. Fluids* **28**, 015112 (2016).
- [20] Y. C. Jung and B. Bhushan, Biomimetic structures for fluid drag reduction in laminar and turbulent flows, *J. Phys.: Condens. Matter* **22**, 035104 (2010).
- [21] H. Ling, S. Srinivasan, K. Golovin, G. H. McKinley, A. Tuteja, and J. Katz, High-resolution velocity measurement in the inner part of turbulent boundary layers over super-hydrophobic surfaces, *J. Fluid Mech.* **801**, 670 (2016).
- [22] H. Park, G. Sun, and C.-J. Kim, Superhydrophobic turbulent drag reduction as a function of surface grating parameters, *J. Fluid Mech.* **747**, 722 (2014).
- [23] C. Peguero and K. Breuer, in *Advances in Turbulence XII*, edited by B. Eckhardt (Springer, Berlin, Heidelberg, 2009), pp. 233.
- [24] S. Srinivasan, J. A. Kleingartner, J. B. Gilbert, R. E. Cohen, A. J. B. Milne, and G. H. McKinley, Sustainable Drag Reduction in Turbulent Taylor-Couette Flows by Depositing Sprayable Superhydrophobic Surfaces, *Phys. Rev. Lett.* **114**, 014501 (2015).
- [25] H. Tian, J. Zhang, E. Wang, Z. Yao, and N. Jiang, Experimental investigation on drag reduction in turbulent boundary layer over superhydrophobic surface by TRPIV, *Theor. Appl. Mech. Lett.* **5**, 45 (2015).
- [26] B. Woolford, J. Prince, D. Maynes, and B. W. Webb, Particle image velocimetry characterization of turbulent channel flow with rib patterned superhydrophobic walls, *Phys. Fluids* **21**, 085106 (2009).
- [27] J. Zhang, H. Tian, Z. Yao, P. Hao, and N. Jiang, Mechanisms of drag reduction of superhydrophobic surfaces in a turbulent boundary layer flow, *Exp. Fluids* **56**, 1 (2015).
- [28] J. Zhao, X. Du, and X. Shi, Experimental research on friction-reduction with super-hydrophobic surfaces, *J. Mar. Sci. Appl.* **6**, 58 (2007).
- [29] H. Haibao, D. Peng, Z. Feng, S. Dong, and W. Yang, Effect of hydrophobicity on turbulent boundary layer under water, *Exp. Therm. Fluid Sci.* **60**, 148 (2015).
- [30] C. G. Jiang, S. C. Xin, and C. W. Wu, Drag reduction of a miniature boat with superhydrophobic grille bottom, *AIP Adv.* **1**, 032148 (2011).
- [31] H. Y. Dong, M. J. Cheng, Y. J. Zhang, H. Wei, and F. Shi, Extraordinary drag-reducing effect of a superhydrophobic coating on a macroscopic model ship at high speed, *J. Mater. Chem. A* **1**, 5886 (2013).
- [32] S. S. Zhang, X. Ouyang, J. Li, S. Gao, S. H. Han, L. H. Liu, and H. Wei, Underwater drag-reducing effect of superhydrophobic submarine model, *Langmuir* **31**, 587 (2015).
- [33] H. Y. Erbil, A. L. Demirel, Y. Avci, and O. Mert, Transformation of a simple plastic into a superhydrophobic surface, *Science* **299**, 1377 (2003).

- [34] A. Tuteja, W. Choi, M. Ma, J. M. Mabry, S. A. Mazzella, G. C. Rutledge, G. H. McKinley, and R. E. Cohen, Designing superoleophobic surfaces, *Science* **318**, 1618 (2007).
- [35] T. L. Liu and C.-J. Kim, Turning a surface superrepellent even to completely wetting liquids, *Science* **346**, 1096 (2014).
- [36] C. Lee and C.-J. Kim, Underwater Restoration and Retention of Gases on Superhydrophobic Surfaces for Drag Reduction, *Phys. Rev. Lett.* **106**, 14502 (2011).
- [37] C. Lee, C.-H. Choi, and C.-J. Kim, Structured Surfaces for a Giant Liquid Slip, *Phys. Rev. Lett.* **101**, 64501 (2008).
- [38] H. Park, Ph.D. dissertation, University of California, Los Angeles (UCLA), 2015.
- [39] B. Emami, A. Hemeda, M. Amrei, A. Luzar, M. Gad-el-Hak, and H. V. Tafreshi, Predicting longevity of submerged superhydrophobic surfaces with parallel grooves, *Phys. Fluids* **25**, 062108 (2013).
- [40] R. Poetes, K. Holtzmann, K. Franze, and U. Steiner, Metastable Underwater Superhydrophobicity, *Phys. Rev. Lett.* **105**, 166104 (2010).
- [41] C. Lee and C.-J. Kim, Wetting and active dewetting processes of hierarchically constructed superhydrophobic surfaces fully immersed in water, *J. Microelectromech. Syst.* **21**, 712 (2012).
- [42] M. Xu, Ph.D. Dissertation, University of California, Los Angeles (UCLA), 2017.
- [43] J. Li, W. Yu, D. Zheng, X. Zhao, C.-H. Choi, and G. Sun, Hot embossing for whole Teflon superhydrophobic surfaces, *Coatings* **8**, 227 (2018).
- [44] RUST-OLEUM, NeverWet Instruction Sheet (2017).
- [45] K. B. Golovin, J. W. Gose, M. Perlin, S. L. Ceccio, and A. Tuteja, Bioinspired surfaces for turbulent drag reduction, *Philos. Trans. R. Soc. A* **374**, 20160189 (2016).
- [46] M. Xu, B. Arihara, H. Tong, N. Yu, Y. Ujiie, and C.-J. Kim, A low-profile wall shear comparator to mount and test surface samples, *Exp. Fluids* **61**, 82 (2020).
- [47] M. MacLean and J. A. Schetz, Numerical study of detailed flow affecting a direct measuring skin-friction gauge, *AIAA J.* **41**, 1271 (2003).
- [48] H. Schlichting, *Boundary-layer Theory* (McGraw-Hill, New York, 1979), 7th ed.
- [49] See Supplemental Material at <http://link.aps.org/supplemental/10.1103/PhysRevApplied.13.034056> for movies of SHPo surfaces during testing.
- [50] H. Park, H. Park, and J. Kim, A numerical study of the effects of superhydrophobic surface on skin-friction drag in turbulent channel flow, *Phys. Fluids* **25**, 110815 (2013).
- [51] M. Gad-el-Hak, Comment on “Experimental study of skin friction drag reduction on superhydrophobic flat plates in high Reynolds number boundary layer flow”, *Phys. Fluids* **25**, 079102 (2013).